









RESEARCH ARTICLE | AUGUST 12 2025

Asymmetric electronic band alignment and potentially enhanced thermoelectric properties in phase-separated Mg_2X ($\text{X} = \text{Si}, \text{Ge}, \text{Sn}$) alloys

Byungki Ryu ; Samuel Foster ; Eun-Ae Choi ; Sungjin Park ; Jaywan Chung ; Johannes de Boer ; Pawel Ziolkowski ; Eckhard Müller ; Seung Zeon Han; SuDong Park ; Neophytos Neophytou  



J. Appl. Phys. 138, 065104 (2025)

<https://doi.org/10.1063/5.0285042>



Articles You May Be Interested In

Defect and phase stability of solid solutions of Mg_2X with antifluorite structure. An ab-initio study

AIP Conf. Proc. (June 2012)

Experimental investigation of the predicted band structure modification of Mg_2X ($\text{X}: \text{Si}, \text{Sn}$) thermoelectric materials due to scandium addition

J. Appl. Phys. (June 2019)

Thermoelectric properties of Mg_2X ($\text{X} = \text{Si}, \text{Ge}$) based bulk and quantum well systems

J. Appl. Phys. (January 2017)



Nanotechnology & Materials Science



Optics & Photonics



Impedance Analysis



Scanning Probe Microscopy



Sensors



Failure Analysis & Semiconductors



Unlock the Full Spectrum.
From DC to 8.5 GHz.

Your Application. Measured.

Find out more



Asymmetric electronic band alignment and potentially enhanced thermoelectric properties in phase-separated Mg_2X ($\text{X} = \text{Si}, \text{Ge}, \text{Sn}$) alloys

Cite as: J. Appl. Phys. 138, 065104 (2025); doi: 10.1063/5.0285042

Submitted: 12 June 2025 · Accepted: 22 July 2025 ·

Published Online: 12 August 2025



Byungki Ryu,^{1,2,a)} Samuel Foster,³ Eun-Ae Choi,⁴ Sungjin Park,¹ Jaywan Chung,¹ Johannes de Boer,^{5,6} Pawel Ziolkowski,⁵ Eckhard Müller,^{5,7} Seung Zeon Han,³ SuDong Park,¹ and Neophytos Neophytou^{3,a)}

AFFILIATIONS

¹Energy Conversion Research Center, Electrical Materials Research Division, Korea Electrotechnology Research Institute (KERI), Changwon 51543, Republic of Korea

²Electric Energy and Materials Engineering, School of KERI, University of Science and Technology, Changwon 51543, Republic of Korea

³School of Engineering, University of Warwick, Coventry CV4 7AL, United Kingdom

⁴Extreme Materials Research Institute, Korea Institute of Materials Science (KIMS), Changwon 51508, Republic of Korea

⁵German Aerospace Center (DLR), Institute for Frontier Materials on Earth and in Space, 51170 Cologne, Germany

⁶Faculty of Engineering, Institute of Technology for Nanostructures (NST) and CENIDE, University of Duisburg-Essen, Building BA, Bismarckstr. 81, D-47057 Duisburg, Germany

⁷Institute of Inorganic and Analytical Chemistry, Justus Liebig University, 35392 Giessen, Germany

^{a)}Authors to whom correspondence should be addressed: byungkiryu@keri.re.kr and n.neophytou@warwick.ac.uk

ABSTRACT

The Mg_2X ($\text{X} = \text{Si}, \text{Ge}, \text{Sn}$) based alloy is an eco-friendly thermoelectric material for mid-temperature applications. The $\text{Mg}_2\text{Si}_{1-x}\text{Sn}_x$ and $\text{Mg}_2\text{Ge}_{1-x}\text{Sn}_x$ alloys can be phase-separated into Si(Ge)- and Sn-rich phases during material synthesis, leading to a nanocomposite with locally varying electronic band structures. First-principles calculations reveal that the valence band offset is eight-times larger than the conduction band offset at the interface between Si- and Sn-rich phases for $x = 0.6$, showing type I and asymmetric band alignment (0.092 vs 0.013 eV). Using the Boltzmann transport theory and thermionic emission calculations, we show that the large valence band energy discontinuity could allow for energy filtering effects to take place that can potentially increase the power factor substantially in the p -type material system if designed appropriately.

© 2025 Author(s). All article content, except where otherwise noted, is licensed under a Creative Commons Attribution (CC BY) license (<https://creativecommons.org/licenses/by/4.0/>). <https://doi.org/10.1063/5.0285042>

I. INTRODUCTION

Mg_2Si -based thermoelectric alloys (Mg_2X , $\text{X} = \text{Si}, \text{Ge}, \text{Sn}$, and their alloys), consisting of non-toxic and earth-abundant elements, have garnered much attention owing to their high n -type ZT in the mid-temperature range (600–800 K).^{1–3} From thermodynamic calculations and some of the experimental data, there exists a large composition range where Mg_2Si – Mg_2Sn (or Mg_2Ge – Mg_2Sn) alloys are immiscible, with the extent of this miscibility gap decreasing

with increasing temperature due to entropy.^{4–7} On the other hand, single phase materials have repeatedly been synthesized within the predicted miscibility gap.^{8–10} It has been argued that coherent interfaces formed during synthesis stabilize the material against unmixing and that breaking this coherence can be an experimentally feasible path to trigger and influence the alloy nanostructuring.^{6,11} As a result, by adjusting processing conditions (e.g., temperature), these alloys can be transformed into Si-rich

$\text{Mg}_2\text{Si}_{1-x}\text{Sn}_x$ and Sn-rich $\text{Mg}_2\text{Si}_{1-x}\text{Sn}_x$ phases due to the miscibility gap, forming an interface-rich microstructure, which can be an effective method to generate a complex nanostructure for phonon scattering, leading to a reduced thermal conductivity.¹²

In general, interfaces also control charge transport depending on the band offset and charge carrier energy (position of the Fermi level η_F),¹³ which often proves beneficial for improving the performance of various electrical and optical devices, and solar cells.^{14–16} Similarly, in thermoelectric materials, although the electrical conductivity can suffer, the interfacial energy barriers at the phase boundaries could play a critical role in thermoelectric transport via energy filtering^{17–22} and bipolar transport suppression.^{23–26} Despite the current large interest in the bulk Mg_2X alloy systems and some early experimental work probing for energy filtering,²⁷ there are only limited reports on the band alignment of the Mg_2Si – Mg_2Sn alloy system and how that can prove beneficial to its thermoelectric properties. Hence, the role of interfaces on the electronic transport in this system is not well understood at present.

In this paper, we report on the theoretical results for the *electronic band energy alignment* between phase-separated $\text{Mg}_2\text{Si}_{1-x}\text{Sn}_x$ alloys and its potential effect on thermoelectric transport (power factor) across the phase boundaries. From first-principles calculations, we find an *asymmetric* band offset with type I band alignment between Si- and Sn-rich $\text{Mg}_2(\text{Si},\text{Sn})$ phases. Using Boltzmann transport theory and thermionic emission, we show that the phase-separated alloy system can provide energy filtering and enhanced power factors (PFs) for the *p*-type system due to the large valence band energy discontinuity.

II. CALCULATION METHOD

We performed first-principles density-functional theory (DFT)^{28,29} calculations for atomic and electronic structures of Mg_2X using projector-augmented wave pseudopotentials^{30,31} and generalized-gradient approximation (GGA),³² as implemented in the Vienna *Ab initio* Simulation Package (VASP) code.^{33,34} We fully optimized the atomic structure within GGA calculations structures, while the lattice parameters of the solid-solution supercells were interpolated using those of the corresponding binary phases. The mixing energies of $\text{Mg}_2(\text{Si},\text{Sn})$ solid solutions were calculated compared to ideal binary phases of Mg_2Si and Mg_2Sn , and the miscibility gap was predicted with the inclusion of an ideal configuration entropy. To obtain reliable electronic structures, we also carried out many-body perturbation theory (MBPT) non-self-consistent G_0W_0 approximation calculations for bulk Mg_2Si , Mg_2Ge , and Mg_2Sn on top of the hybrid-DFT.³⁵ For this, we employed the HSE06 functional with the exchange mixing parameter of 35% and screening parameter of 0.2 \AA^{-1} (Refs. 35 and 36), hereafter referred to as HSE-35. The details for band structure calculations can be found in a previous report.³⁶ Note that spin-orbit interaction (SOI) is included for all electronic structure calculations.

For the band alignment of Mg_2X alloys and related materials, the reference potential method^{37–41} was applied on the ideal 16-layer (110) Mg_2X surface structures. We extracted the reference potential of Mg_2X surface structures with respect to the vacuum energy. For simplicity, the strain on bulk and interfaces is neglected. By aligning the G_0W_0 corrected bulk band edge energies

on the DFT surface reference potential,^{38,41} the band edge energies are aligned with the zero vacuum level. For the ternary alloys, energies of one valence band and two conduction band minima were linearly interpolated with composition to predict the composition-dependent band structure. Around the conduction band convergence composition, the two conduction bands cross and then separate again. Considering the character of each band, we tracked the evolution of each band edge individually and performed interpolations accordingly.

III. RESULTS AND DISCUSSION

Figures 1(a) and 1(b) show the atomic structures of the 96-atom supercells for binary Mg_2Si and solid-solution $\text{Mg}_2\text{Si}_{0.59}\text{Sn}_{0.41}$. The ideal Mg_2X compounds have an anti-fluorite structure, where the anion X atoms are positioned at the FCC regular sites and the cation Mg atoms are positioned at the tetrahedral interstitial sites. In this configuration, each X anion atom is surrounded by eight Mg atoms. We used the optimized lattice parameters of 6.348, 6.410, and 6.801 Å for Mg_2Si , Mg_2Ge , and Mg_2Sn , as predicted by the previous study.³⁶ We modeled the solid solution of ternary $\text{Mg}_2(\text{Si}_{1-x}\text{Sn}_x)$ by assuming a random substitution of Si and Sn atoms at the X sites, with the lattice parameter linearly interpolated between those of Mg_2Si and Mg_2Sn . After structural relaxation, the positions of Mg, Si, and Sn elements were displaced from the ideal positions.

Figure 1(c) quantifies the structural disorder in solid-solution models using the root-mean-square (RMS) displacement, defined as the atomic position displacement from their ideal lattice sites after relaxation. On average, the RMS displacement was smaller than 0.06 Å. Mg exhibits the largest displacement, followed by Si. Sn atoms show relatively small displacement for composition $x < 0.6$, but is comparable to that of Si when $x > 0.6$.

Figure 2 shows the DFT-based predictions of the thermodynamic stability and phase diagram of $\text{Mg}_2(\text{Si},\text{Sn})$. The Mg_2Si and Mg_2Sn alloys are immiscible at 0 K, but their alloy becomes miscible at elevated temperatures. A randomly generated supercell structure of $\text{Mg}_2(\text{Si},\text{Sn})$ exhibits a positive mixing energy (E_{mix}), consistent with the immiscibility reported in the phase diagram and various literature reports.^{4,5,42} However, when sufficient thermal energy is available, a solid solution can form. To quantitatively analyze the thermodynamic within the DFT framework, we incorporate an ideal configuration entropy (S_{mix}), assuming an ideal solid solution. The temperature-dependent mixing free energy is calculated as

$$E_{\text{mix}} = E[\text{Mg}_2\text{Si}_{1-x}\text{Sn}_x] - \{(1-x) \cdot E[\text{Mg}_2\text{Si}] + x \cdot E[\text{Mg}_2\text{Sn}]\}, \quad (1)$$

$$\frac{S_{\text{mix}}(x)}{k_B} = \Sigma(-p_i \ln(p_i)) \approx -x \ln(x) - (1-x) \ln(1-x), \quad (2)$$

$$F_{\text{mix}} = E_{\text{mix}} - TS_{\text{mix}}. \quad (3)$$

Figure 2(a) shows the calculated mixing energy E_{mix} for $\text{Mg}_2(\text{Si}_{1-x}\text{Sn}_x)$ alloys obtained from DFT calculations with respect

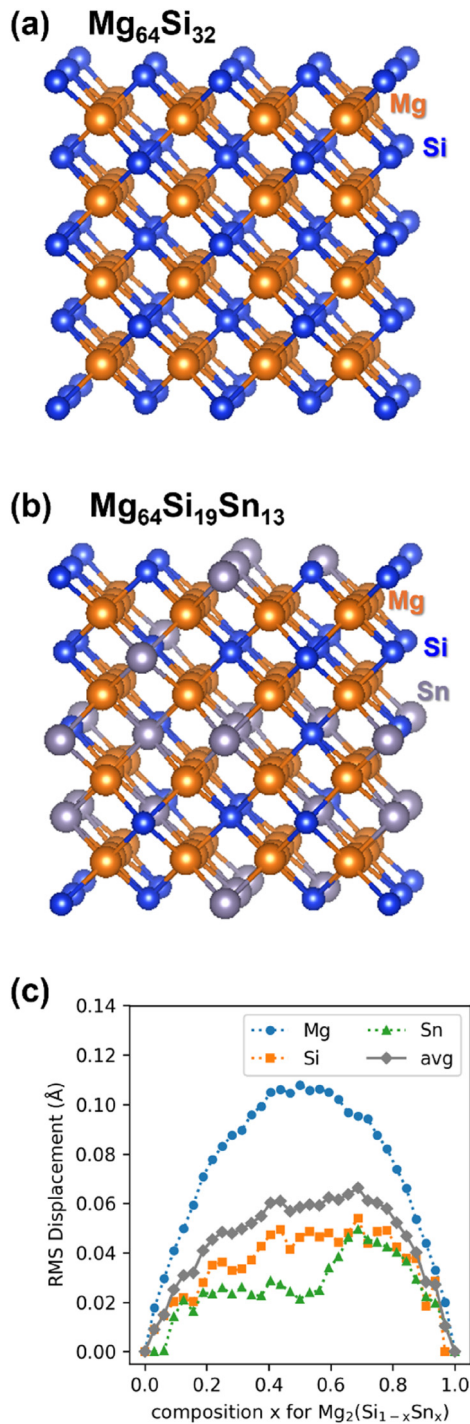


FIG. 1. Atomic structure and displacement behavior of the $\text{Mg}_2\text{Si}_{1-x}\text{Sn}_x$ solid-solution model. Supercell models of (a) $\text{Mg}_{64}\text{Si}_{32}$ representing for binary Mg_2Si and (b) $\text{Mg}_{64}\text{Si}_{19}\text{Sn}_{13}$ representing for $\text{Mg}_2\text{Si}_{0.59}\text{Sn}_{0.41}$ solid solution. (c) Calculated root-mean-square displacement of Mg, Si, and Sn atoms vs composition x in $\text{Mg}_2\text{Si}_{1-x}\text{Sn}_x$, along with the average displacement.

to two end members, Mg_2Si and Mg_2Sn . E_{mix} exceeds 40 meV per formula unit at intermediate compositions, indicating strong immiscibility at low temperatures. E_{mix} and F_{mix} were fitted to a fourth-degree polynomial. Figure 2(b) shows the temperature-dependent mixing free energy. As temperature increases, the entropic contribution lowers the free energy, thereby stabilizing the solid-solution state.

At 700 K, shown in Fig. 2(c), the F_{mix} becomes negative near the Si-rich ($x < 0.1$) and Sn-rich ($x > 0.9$) ends, suggesting that phase coexistence of two different compositions is thermodynamically favorable, consistent with a previous work, but with different compositions.⁷ The double well shape of the free energy curve indicates the possibility of phase separation with intermediate compositions. The binodal points, marked by filled circles, represent the boundaries of two-phase region and are determined from the common tangent construction,

$$\left. \frac{\partial F}{\partial x} \right|_{x=x_{1b}} = \left. \frac{\partial F}{\partial x} \right|_{x=x_{2b}}. \quad (4)$$

The derivative of the free energy with respect to composition corresponds to the chemical potential. Thus, the binodal points represent compositions at which two phases coexist in equilibrium with equal chemical potentials. The spinodal points, marked by open stars, correspond to inflection points of the free energy curve, where the second derivative vanishes,

$$\left. \frac{\partial^2 F}{\partial x^2} \right|_{x_{1s}} = \left. \frac{\partial^2 F}{\partial x^2} \right|_{x_{2s}} = 0. \quad (5)$$

When the curvature of the free energy (the second derivative) is positive, the system is locally stable against small perturbations in the composition. However, inside the spinodal region, where the curvature becomes negative, the system is unstable with respect to such compositional fluctuations, and spinodal decomposition occurs. Figure 2(d) summarizes the temperature-dependent phase diagram with binodal and spinodal boundaries. The binodal gap is wider than the spinodal gap. For instance, at 1200 K, a two-phase region exists between Si-rich $\text{Mg}_2\text{Si}_{0.6}\text{Sn}_{0.4}$ and Sn-rich $\text{Mg}_2\text{Si}_{0.4}\text{Sn}_{0.6}$. As temperature decreases, the miscibility gap widens. Below 400 K, the two binaries are nearly completely immiscible. Although the spinodal decomposition gap is relatively large, the second derivative of free energy remains nearly constant over a wide composition range. This implies that small compositional fluctuations within the spinodal region do not significantly lower the free energy, supporting the likelihood of a de-mixed two-phase state in Mg–Si–Sn alloys.

Table I summarizes the bandgap values for the Mg_2Si , Mg_2Ge , and Mg_2Sn obtained from various calculation methods and experimental measurement techniques. Within density-functional theory-Perdew–Burke–Ernzerhof (DFT-PBE), these binary compounds have bandgaps smaller than 0.2 eV, indicating a narrow bandgap semiconductor. When more advanced calculation methods such as hybrid-DFT or GW many-body approaches are employed,^{36,43,44} the calculated bandgaps show much better agreement with experimental values.^{45–48}

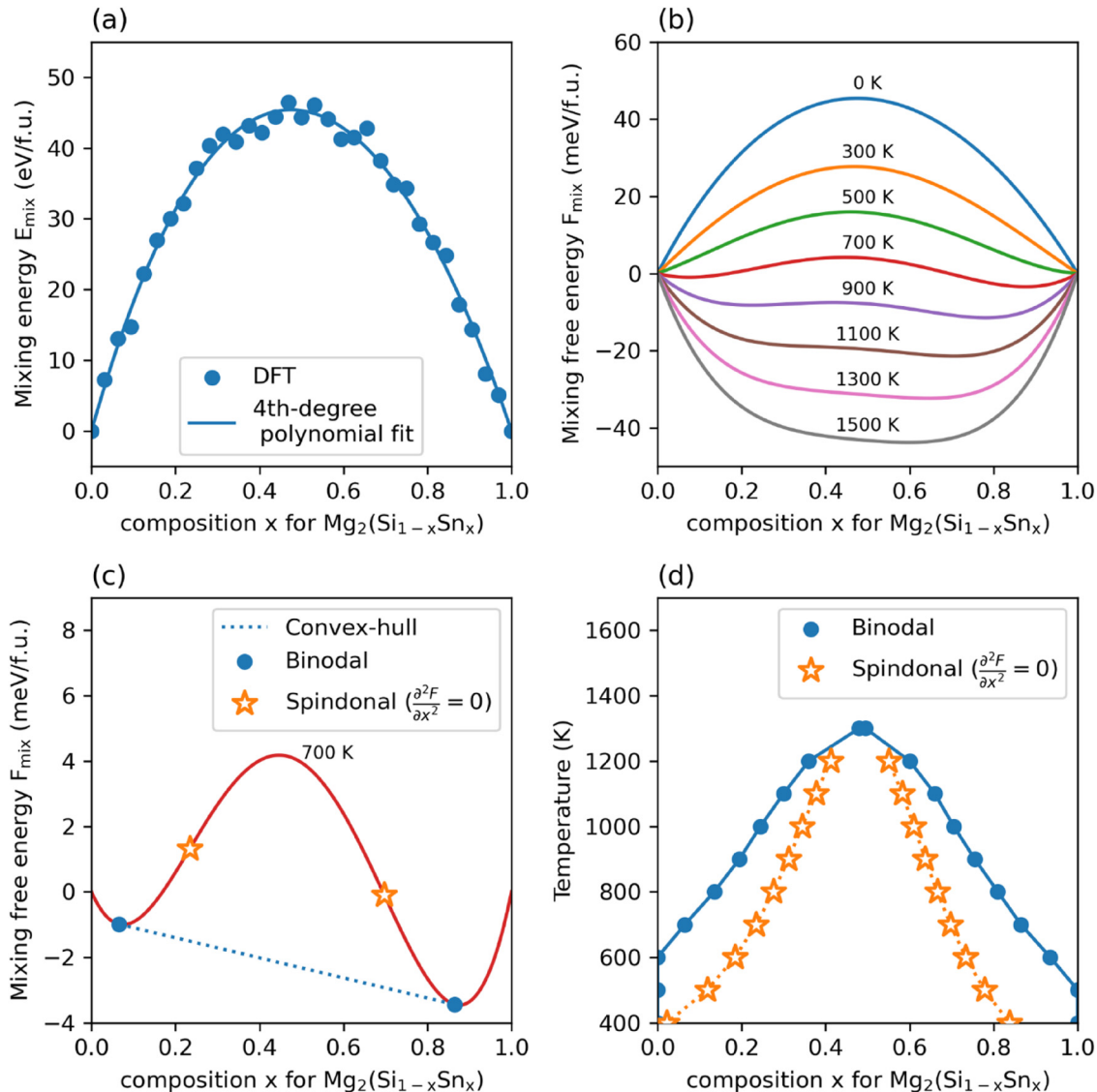


FIG. 2. DFT-based prediction of the thermodynamic stability and phase diagram of $\text{Mg}_2\text{Si}_{1-x}\text{Sn}_x$ alloy systems. (a) E_{mix} and (b) temperature-dependent F_{mix} curves with a fourth-degree polynomial fit. (c) Free energy at 700 K with binodal points from the convex hull and spinodal points from inflection points. (d) Calculated phase diagram showing binodal and spinodal boundaries over temperature.

Figures 3(a) and 3(b) show the calculated electronic band alignment for the Mg_2Si , Mg_2Ge , and Mg_2Sn binaries with respect to the vacuum energy levels. In DFT calculations, the band alignment is not reliable due to the well-known bandgap underestimation issue. For Mg_2Sn , the DFT bandgap is even negative, inconsistent with previous observations.^{44,45} To overcome this, we calculated the band alignment using MBPT G_0W_0 calculations, which provide corrected bandgaps for Mg_2X . Finally, a type I band alignment, where both the conduction and valence band edges of one component lie within the bandgap of the other, is obtained.

The alignment is also asymmetric due to the different offsets at the conduction and valence band edges, as shown in Fig. 3(b). The conduction band offset (CBO) is smaller than the valence band offset (VBO). In the MBPT G_0W_0 calculations, the corrected CBM energy of Mg_2Si (Mg_2Ge) was calculated to be 0.13 eV (0.10 eV), and the VBM of Mg_2Si (Mg_2Ge) was calculated to be -0.46 eV (-0.42 eV) with respect to the CBM (VBM) of Mg_2Sn , respectively.

Figure 3(c) shows the electronic band alignment for $\text{Mg}_2\text{Si}_{1-x}\text{Sn}_x$ ternaries and related materials. For the Si- and Sn-rich phases of $\text{Mg}_2(\text{Si},\text{Sn})$, we consider the $\text{Mg}_2\text{Si}_{0.6}\text{Sn}_{0.4}$ and

TABLE I. Summary of bandgap values for Mg₂Si, Mg₂Ge, and Mg₂Sn compounds obtained from different theoretical approaches (DFT, hybrid functionals, GW) and experimental techniques (optical absorption and transport measurements).

Method, Reference		Bandgap (eV)		
		Mg ₂ Si	Mg ₂ Ge	Mg ₂ Sn
Theory	PBE with SOI (calculated lattice), this work and Ref. 36	0.191	0.090	−0.346
	HSE-25 (calculated lattice), this work and Ref. 36	0.568	0.523	0.146
	HSE-25 (experimental lattice) ⁴³	0.570	...	0.145
	HSE-35 with SOI (calculated lattice), this work and Ref. 36	0.715	0.617	−0.030
	G ₀ W ₀ on top of HSE-25 with SOI (calculated lattice) ³⁶	0.763	0.690	0.077
	G ₀ W ₀ on top of HSE-30 with SOI (calculated lattice) ³⁶	0.798	0.724	0.177
	G ₀ W ₀ on top of HSE-35 with SOC (calculated lattice), this work and Ref. 36	0.835	0.759	0.244
	GW + SOI ⁴⁴	0.728	0.555	0.142
Experiment	Optical, absorption coeff. ⁴⁵	0.623	0.595	...
	Logarithmic plot of electrical resistivity ⁴⁶	0.71	0.54	...
	Infrared absorption, T-dep ⁴⁷	...	0.57	...
	Infrared absorption, T-dep ⁴⁸	0.22–0.30

Mg₂Si_{0.4}Sn_{0.6} compositions. These compositions correspond to the binodal points at 1200 K, where phase separation into Si-rich and Sn-rich domains is thermodynamically favorable according to the calculated phase diagram. It is worth noting that we interpolated the conduction band energies of the X₁ and X₃ states in binary Mg₂Si and Mg₂Sn and obtained the CBM energy of the solid-solution states by considering the band crossing between X₁ and X₃ in Mg₂(Si,Sn) alloys. From the MBPT G₀W₀ calculations, the CBO at the interface between Sn-rich Mg₂Si_{0.4}Sn_{0.6} and Si-rich Mg₂Si_{0.6}Sn_{0.4} phases is relatively small (0.013 eV), whereas the VBO is larger (0.092 eV). We also compare the relative band alignment between Mg₂X and related elemental materials: Mg₂Si, Si-rich Mg₂(Si,Sn), Sn-rich Mg₂(Si,Sn), Mg₂Sn, metallic Mg, semiconducting Si and Ge in the diamond structure, and metallic Sn. For the metallic elements, we used their experimental work functions: 3.68 eV for Mg and 4.42 eV for Sn.⁴¹ For the semiconducting element phases, we use the reported band alignment values: 3.7 eV for n-type Si and 3.5 eV for n-type Ge.⁴⁹ Interestingly, we also find an asymmetric behavior between Mg₂X and X elements. Other than for Sn, the CBMs and Fermi level of metals are more aligned, compared to their VBMs.

In Mg₂(Si,Sn) alloys, the conduction band convergence of the X₁ and X₃ CBM states is known to be the origin of the high power factor in the n-type system.^{8,36} Furthermore, the significant change in the valence band edge energies between the Mg₂X based binary and ternary alloys could suggest an additional mechanism for enhanced thermoelectric performance in the phase-separated *p*-type Mg₂Si–Mg₂Sn alloys. The band offset magnitudes of Si- and Sn-rich phases are large enough to be able to act as barriers for carrier energy filtering in the case of *p*-type transport.²²

To provide a first-order upper level estimate of the power factor improvement that filtering can allow in the phase-separated Mg₂Si_{0.4}Sn_{0.6}/Mg₂Si_{0.6}Sn_{0.4} alloy system compared to the single phase Mg₂Si_{0.4}Sn_{0.6} (the one with the lowest bandgap, which will act as the base material reference), we performed transport calculations based on the Boltzmann transport equation (BTE). To

simplify the transport treatment, we assume that it is dominated by elastic, isotropic scattering mechanisms (like acoustic-phonon scattering^{10,50}), which allows the use of simplified expressions for the scattering rates. In the BTE, the transport coefficients are given by

$$\sigma = R^{(0)}, \quad (6)$$

$$S = \frac{k_B R^{(1)}}{q_0 R^{(0)}}, \quad (7)$$

$$\kappa_e = \frac{k_B^2 T}{q_0^2} \left[R^{(2)} - \frac{[R^{(1)}]^2}{R^{(0)}} \right], \quad (8)$$

where

$$R^{(\alpha)} = q_0^2 \int_{E_0}^{\infty} dE \left(-\frac{\partial f_0}{\partial E} \right) G(E) \left(\frac{E - E_F}{k_B T} \right)^\alpha, \quad (9)$$

with the energy-dependent transport distribution function defined as

$$G(E) = \tau_s(E) v^2(E) g(E). \quad (10)$$

Above $\tau_s(E)$ is the relaxation time, $v(E)$ is the carrier velocity, and $g(E)$ is the density of states of the material. For simplicity, we assume parabolic effective mass bands with a global $m^* = 0.5m_0$ in all instances. We also assumed a constant (in energy) mean-free-path (MFP), i.e., $mfp = \tau_s(E) v(E) = 10$ nm, which infers acoustic-phonon-scattering-limited transport (without loss in generality here). Here, the used *mfp* value (10 nm) is comparable to those typically observed in phonon-limited transport regimes of conventional semiconductors. We do not have precise information on the *mfp* of the Mg₂(Si,Sn) alloys, nor do we explicitly account for phonon scattering mechanisms such as ionized impurity scattering, boundary scattering, or alloy disorder

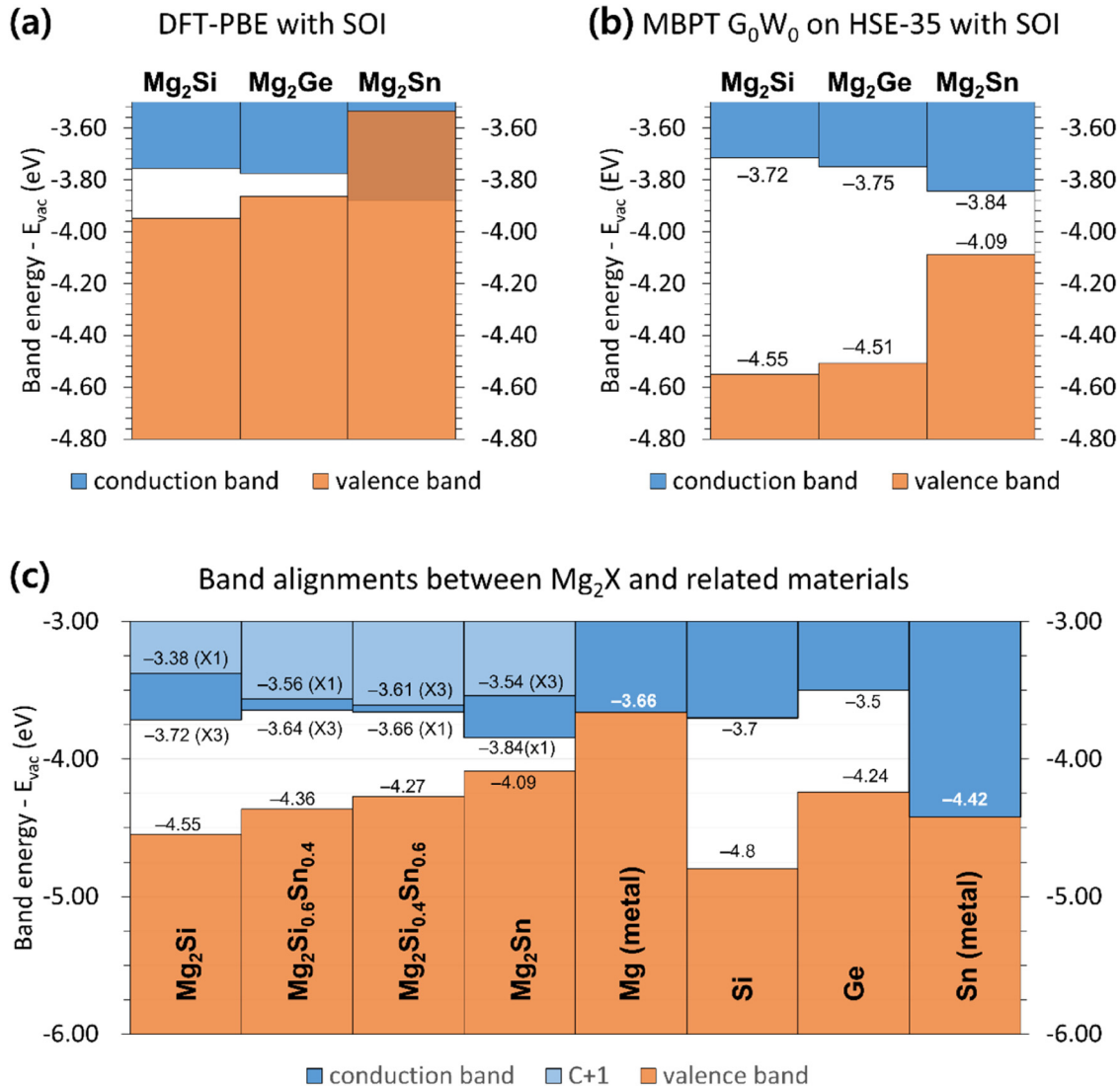


FIG. 3. Electronic band alignment for Mg₂X (X = Si, Ge, Sn) obtained using (a) the DFT-PBE calculations with SOI and (b) the MBPT G₀W₀ calculations on top of HSE35 with SOI calculations. In (c), the band edge positions of Mg₂X-related ternary alloys are shown and compared with the related elements. For alignment, the vacuum energy level is set to zero.

scattering mechanisms. Thus, our results should only provide qualitative estimates, rather than quantitative predictions, but still they will point toward an upper limit PF improvement estimation (at first order).

In order to cover the different length scales that the two different phases can have and how these will affect the TE performance, we assume two situations: (i) the individual phase domains are large regions, much larger compared to the characteristic lengths of electron momentum and energy relaxation. In this case, the charge carriers are in equilibrium in each region, and a series resistance model can be employed. At the first order, the electronic

conductivity and Seebeck coefficient in a two-phase material are given by

$$\frac{\nu_{\text{tot}}}{\sigma_{\text{tot}}} = \frac{V_1}{\sigma_1} + \frac{V_2}{\sigma_2}, \quad (11)$$

$$S_{\text{tot}} = \frac{S_1 V_1 + S_2 V_2}{V_1 + V_2}, \quad (12)$$

where the total is given by combinations of the individual phase

components, weighted by the volume of the different phases (which in this case we assume for them to be equal).

In the second scenario, we assume that the individual phase regions are small, to enable non-equilibrium transport and enable an effective energy filtering design mechanism as described in our previous works.^{51,52} In this case, we assume that the barrier regions are narrow enough to enable thermionic emission without the carrier energies relaxing on the barriers, while the wells are of the order of the energy relaxation length of the carriers such that they do not relax their energy in the wells. In this case, high energy (hot), high velocity, and high mobility carriers are injected from the barriers over the wells, while the low energy, cold carriers are blocked. The latter increases the Seebeck coefficient, which is retained high in both the barriers and wells, as carriers do not relax their energy in the wells. The former allows for retained conductivity (despite the presence of the barriers), because the thermionically emitted carriers are of high velocity and mobility. In the presence of a potential barrier, as is the case at the interfaces between dissimilar materials, in which case potential barriers of height V_B are formed for carriers, it is customary to impose thermionic emission above the barriers, under which the conductivity is given by

$$\sigma(E) = 0 \text{ for } E \leq V_B, \quad (13)$$

$$\sigma(E) = \sigma_0 T_r(E) \text{ for } E > V_B, \quad (14)$$

where $\sigma(E)$ and $\sigma_0(E)$ are the carrier band energy-dependent conductivity with and without potential barriers, respectively, and $T_r(E)$ is the transmission of the charge energy state E (here for simplicity, we assume $T_r(E) = 1$). In this case, transport over the barriers provides energy filtering, which increases the Seebeck coefficient composite.

Thus, we examine two cases: (i) the relative performance of the two-phase system if the phases are large enough such that transport in each phase is resistive and (ii) the relative performance of the p -type system in the presence of energy filtering. This is done in a single way by shifting the Fermi level from the conduction band to the valence band and computing the transport properties. Here, the transport properties of the electron and hole carriers are computed separately and then combined as described in Ref. 26.

Figure 4 shows the TE coefficients (conductivity σ , Seebeck coefficient S , and power factor σS^2) vs the position of the Fermi level η_F for three different cases: (i) the single phase $\text{Mg}_2\text{Si}_{0.4}\text{Sn}_{0.6}$ system, which will act as a reference (black lines), (ii) the $\text{Mg}_2\text{Si}_{0.4}\text{Sn}_{0.6}$ – $\text{Mg}_2\text{Si}_{0.6}\text{Sn}_{0.4}$ two-phase system under resistive transport conditions, assuming that the individual phases are large enough such that charge carriers relax their energies in the bands of the phase and are in near-equilibrium conditions (blue lines), and (iii) the $\text{Mg}_2\text{Si}_{0.4}\text{Sn}_{0.6}$ – $\text{Mg}_2\text{Si}_{0.6}\text{Sn}_{0.4}$ two-phase system, the larger-gap phase $\text{Mg}_2\text{Si}_{0.6}\text{Sn}_{0.4}$ acting as the filtering barrier for holes—a 0.092 eV barrier is formed in the VB and 0.013 eV in the CB (red lines)—in this case, we assume that the phases are short enough such that charge carriers do not fully relax in the wells or the barriers, having non-equilibrium transport features, such that the band discontinuities can act effectively as filtering barriers. This can be typically between 30 nm up to 100 nm in common

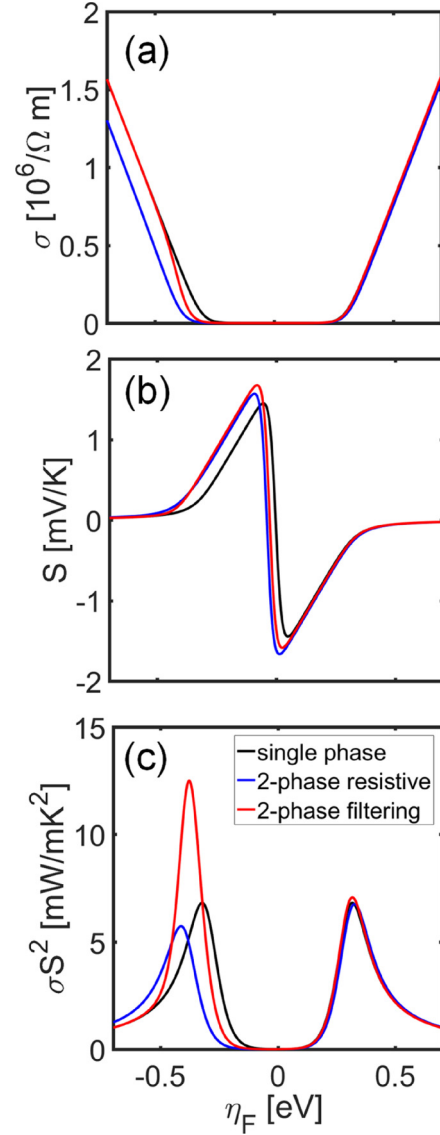


FIG. 4. Thermoelectric coefficients at 300 K. (a) Electrical conductivity, (b) Seebeck coefficient, and (c) power factor vs the position of the Fermi level. Three different cases are shown: (i) the single phase $\text{Mg}_2\text{Si}_{0.4}\text{Sn}_{0.6}$ system (black lines), which acts as a reference, (ii) the two-phase $\text{Mg}_2\text{Si}_{0.4}\text{Sn}_{0.6}/\text{Mg}_2\text{Si}_{0.6}\text{Sn}_{0.4}$ system (blue lines) but under resistive transport conditions (where we assume equal size phases), and (iii) the two-phase $\text{Mg}_2\text{Si}_{0.4}\text{Sn}_{0.6}/\text{Mg}_2\text{Si}_{0.6}\text{Sn}_{0.4}$ system with the $\text{Mg}_2\text{Si}_{0.6}\text{Sn}_{0.4}$ acting as the filtering barrier for holes—a 0.092 eV barrier is formed in the VB and 0.013 eV in the CB (red lines)—in this case, we assume that the phases are short enough such that charge carriers do not fully relax in the wells or the barriers, having non-equilibrium transport features, such that the band discontinuities can act effectively as filtering barriers. This can be typically between 30 nm up to 100 nm in common

semiconductors. All simulations here are performed at a room temperature of $T = 300$ K. We then observed whether the phase-separated alloy system has the ability to improve the PF, in addition to the expected reduction in its thermal conductivity (not examined here).

The conductivity of the three material cases examined has a very similar trend, with the only difference being the onset of the conductivity in the valence band, as modified by the band edge discontinuity [see Fig. 4(a)]. The small differences in the conduction band make the systems behave identically. In the valence band, a sharper slope is acquired by the filtering system (red line), a typical feature of *thermionic emission*.^{51,53} In Fig. 4(b), the Seebeck coefficients of the two-phase systems are shifted toward the left in the valence band, a signature of increased resistance for the resistive system, and energy filtering for the filtering system. The increase in the Seebeck coefficient in regions of steep conductivity slope (red line) provides a large power factor increase as observed in Fig. 4(c). In this case, the PF can double, but this is an upper limit of what can be achieved. In practice, the well/barrier geometry needs to be properly designed in order to retain this value,^{22,26} but in this work, we do not go into those details; we only want to demonstrate that the system at hand (Mg₂Sn/Mg₂Si-based phase-separated alloy system) could have potential for higher *p*-type PFs once designed appropriately to take advantage of energy filtering. Also note that the absolute values for the conductivity and the PF would be overestimated, since we have not included the effect of ionized impurity scattering when we shift the Fermi level into degenerate conditions, and we omit other scattering mechanisms such as optical and polar phonon scattering. Nevertheless, these will be common for all systems, such as the relative performance increase would still be a valid indication of the system behavior.

On the other hand, the resistive system (blue line) has lower PF performance for holes due to the reduction in the conductivity of the higher bandgap phase, and the fact that the regions are assumed large enough such that thermionic emission is absent, and the material reduced to a series resistance system. Here, we are mostly interested in the *p*-type system; however, the large band discontinuity in the VB and its reduced transport under resistive conditions could also lead to reduced electronic thermal conductivity and bipolar transport at high operating temperatures when the *n*-type polarity is considered, beyond the reduction in the lattice thermal conductivity, both of which are beneficial for larger *ZT* (although our calculations for this particular system indicate that the benefits are only marginal due to the relatively large bandgap of 0.61 eV).

Since electronic conduction in the *p*-type system is degraded by the Mg₂Si barrier, for such phase-separated samples, this asymmetric band alignment can be responsible for the experimentally observed low mobility, in addition to the larger valence band mass in *p*-type alloys.^{54,55} In that case, it is suggested that the material is doped to highly degenerate *p*-type conditions such that the Fermi level is pushed into the valence bands closer to the barrier heights formed at the interfaces, and in that case, power factor improvements are possible by taking advantage of filtering effects and high carrier velocities, a design strategy described in detail in Refs. 53 and 56. At the same time, our results also suggest that the asymmetric transport behavior plays a crucial role in metallic or semi-metallic thermoelectrics, consistent with earlier reports. If the system is heavily degenerately doped (deep Fermi level inside a conduction or valence band), the system will be highly metallic, but will still show a high power factor, an unconventional feature compared semiconducting thermoelectrics. As explained in Ref. 57

transport asymmetry is what dictates larger Seebeck coefficients, and these can be achieved even under metallic conditions.⁵⁷ Meanwhile, *p*-type doping is challenging for this alloy.⁵⁸ Nevertheless, if such *p*-doping strategies can be successfully implemented such as using Li impurity doping,^{59,60} they may enable an enhanced power factor through energy filtering and high carrier velocities.

IV. CONCLUSION

In summary, we report on the asymmetric electronic band alignments in Mg₂X (X = Si, Ge, Sn) and their alloys. Owing to the immiscible nature, the Mg₂(Si,Sn) based alloys can be decomposed into Si- and Sn-rich phases at lower temperature range: Mg₂Si_{0.6}Sn_{0.4}–Mg₂Si_{0.4}Sn_{0.6}. In *p*-type alloys, the large valence band offset, which can act as a barrier, could be designed to provide energy filtering capabilities that could ideally provide large power factor improvements.

ACKNOWLEDGMENTS

This work was supported by the Energy Efficiency & Resource Core Technology Program of the Korea Institute of Energy Technology Evaluation and Planning (KETEP) granted from the Ministry of Trade, Industry & Energy (MOTIE), Republic of Korea (Grant No.: 2021202080023D). The work was also supported by the Primary Research Program of KERI through the National Research Council of Science and Technology (NST) funded by the Ministry of Science and ICT (MSIT) of the Republic of Korea (No. 25A01013). B.R., E.-A.C., and S.Z.H. were supported by the National Research Foundation of Korea (NRF) grant funded by the Korea Government (MSIP) (No. 2022M3C1C8093916). J.d.B. was partially funded by the Deutsche Forschungsgemeinschaft (DFG, German Research Foundation) under Project No. 520487260. N.N. received funding from the European Research Council (ERC) under the European Union's Horizon 2020 Research and Innovation Programme (Grant Agreement No. 678763) and from the U.K. Research and Innovation fund (Project Reference No. EP/X02346X/1).

AUTHOR DECLARATIONS

Conflict of Interest

The authors have no conflicts to disclose.

Author Contributions

Byungki Ryu: Conceptualization (equal); Formal analysis (equal); Funding acquisition (equal); Investigation (equal); Methodology (equal); Project administration (equal); Software (equal); Supervision (equal); Validation (equal); Visualization (equal); Writing – original draft (equal); Writing – review & editing (equal). **Samuel Foster:** Formal analysis (equal); Investigation (equal); Methodology (equal); Software (equal). **Eun-Ae Choi:** Formal analysis (equal); Investigation (equal); Methodology (equal); Validation (equal); Writing – review & editing (equal). **Sungjin Park:** Investigation (equal). **Jaywan Chung:** Funding acquisition (equal); Investigation (equal); Methodology (equal);

Project administration (equal); Software (equal); Supervision (equal). **Johannes de Boor**: Conceptualization (equal); Writing – review & editing (equal). **Pawel Ziolkowski**: Funding acquisition (equal); Writing – review & editing (equal). **Eckhard Müller**: Supervision (equal); Writing & review & editing (equal). **Seung Zeon Han**: Conceptualization (equal); Funding acquisition (equal); Investigation (equal); Project administration (equal); Supervision (equal); Writing – review & editing (equal). **SuDong Park**: Conceptualization (equal); Funding acquisition (equal); Investigation (equal); Project administration (equal); Supervision (equal). **Neophytos Neophytou**: Conceptualization (equal); Formal analysis (equal); Funding acquisition (equal); Investigation (equal); Methodology (equal); Project administration (equal); Software (equal); Supervision (equal); Validation (equal); Visualization (equal); Writing – original draft (equal); Writing – review & editing (equal).

DATA AVAILABILITY

The data that support the findings of this study are available from the corresponding authors upon reasonable request: B.R. for band alignments and N.N. for transport calculations.

REFERENCES

- ¹V. K. Zaitsev, M. I. Fedorov, E. A. Gurieva, I. S. Eremin, P. P. Konstantinov, A. Y. Samunin, and M. V. Vedernikov, “Highly effective $\text{Mg}_2\text{Si}_{1-x}\text{Sn}_x$ thermoelectrics,” *Phys. Rev. B* **74**(4), 045207 (2006).
- ²D. M. Rowe, *Thermoelectrics Handbook: Macro to Nano* (CRC/Taylor & Francis, Boca Raton, 2006).
- ³H. J. Goldsmid, *Introduction to Thermoelectricity* (Springer, Berlin, 2016).
- ⁴I.-H. Jung, D.-H. Kang, W.-J. Park, N. J. Kim, and S. Ahn, “Thermodynamic modeling of the Mg–Si–Sn system,” *CALPHAD* **31**(2), 192–200 (2007).
- ⁵A. Kozlov, J. Gröbner, and R. Schmid-Fetzer, “Phase formation in Mg–Sn–Si and Mg–Sn–Si–Ca alloys,” *J. Alloys Compd.* **509**(7), 3326–3337 (2011).
- ⁶S. Yi, V. Attari, M. Jeong, J. Jian, S. Xue, H. Wang, R. Arroyave, and C. Yu, “Strain-induced suppression of the miscibility gap in nanostructured Mg_2Si – Mg_2Sn solid solutions,” *J. Mater. Chem. A* **6**(36), 17559–17570 (2018).
- ⁷M. Yasseri, A. Sankhla, H. Kamila, R. Orenstein, D. Y. N. Truong, N. Farahi, J. de Boor, and E. Mueller, “Solid solution formation in $\text{Mg}_2(\text{Si},\text{Sn})$ and shape of the miscibility gap,” *Acta Mater.* **185**, 80–88 (2020).
- ⁸W. Liu, X. Tan, K. Yin, H. Liu, X. Tang, J. Shi, Q. Zhang, and C. Uher, “Convergence of conduction bands as a means of enhancing thermoelectric performance of n-type $\text{Mg}_2\text{Si}_{1-x}\text{Sn}_x$ solid solutions,” *Phys. Rev. Lett.* **108**(16), 166601 (2012).
- ⁹A. Sankhla, A. Patil, H. Kamila, M. Yasseri, N. Farahi, E. Mueller, and J. de Boor, “Mechanical alloying of optimized $\text{Mg}_2(\text{Si},\text{Sn})$ solid solutions: Understanding phase evolution and tuning synthesis parameters for thermoelectric applications,” *ACS Appl. Energy Mater.* **1**(2), 531–542 (2018).
- ¹⁰H. Kamila, P. Sahu, A. Sankhla, M. Yasseri, H.-N. Pham, T. Dasgupta, E. Mueller, and J. de Boor, “Analyzing transport properties of p-type Mg_2Si – Mg_2Sn solid solutions: Optimization of thermoelectric performance and insight into the electronic band structure,” *J. Mater. Chem. A* **7**(3), 1045–1054 (2019).
- ¹¹M. Yasseri, K. Mitra, A. Sankhla, J. de Boor, and E. Müller, “Influence of Mg loss on the phase stability in Mg_2X (X = Si, Sn) and its correlation with coherency strain,” *Acta Mater.* **208**, 116737 (2021).
- ¹²Q. Zhang, J. He, T. J. Zhu, S. N. Zhang, X. B. Zhao, and T. M. Tritt, “High figures of merit and natural nanostructures in $\text{Mg}_2\text{Si}_{0.4}\text{Sn}_{0.6}$ based thermoelectric materials,” *Appl. Phys. Lett.* **93**(10), 102109 (2008).
- ¹³B. Ryu, H.-K. Noh, E.-A. Choi, and K. J. Chang, “O-vacancy as the origin of negative bias illumination stress instability in amorphous In–Ga–Zn–O thin film transistors,” *Appl. Phys. Lett.* **97**(2), 022108 (2010).
- ¹⁴J. Robertson, “Band offsets of wide-band-gap oxides and implications for future electronic devices,” *J. Vac. Sci. Technol. B* **18**(3), 1785–1791 (2000).
- ¹⁵K. (Albert) Wang, C. Lian, N. Su, D. Jena, and J. Timler, “Conduction band offset at the InN/GaN heterojunction,” *Appl. Phys. Lett.* **91**(23), 232117 (2007).
- ¹⁶T. Minemoto, T. Matsui, H. Takakura, Y. Hamakawa, T. Negami, Y. Hashimoto, T. Uenoyama, and M. Kitagawa, “Theoretical analysis of the effect of conduction band offset of window/CIS layers on performance of CIS solar cells using device simulation,” *Sol. Energy Mater. Sol. Cells* **67**(1), 83–88 (2001).
- ¹⁷J. P. Heremans, C. M. Thrush, and D. T. Morelli, “Thermopower enhancement in PbTe with Pb precipitates,” *J. Appl. Phys.* **98**(6), 063703 (2005).
- ¹⁸J. M. O. Zide, D. Vashaee, Z. X. Bian, G. Zeng, J. E. Bowers, A. Shakouri, and A. C. Gossard, “Demonstration of electron filtering to increase the Seebeck coefficient in $\text{In}_{0.53}\text{Ga}_{0.47}\text{As}/\text{In}_{0.53}\text{Ga}_{0.28}\text{Al}_{0.19}\text{As}$ superlattices,” *Phys. Rev. B* **74**(20), 205335 (2006).
- ¹⁹S. V. Faleev and F. Léonard, “Theory of enhancement of thermoelectric properties of materials with nanoinclusions,” *Phys. Rev. B* **77**(21), 214304 (2008).
- ²⁰M. Zebarjadi, K. Esfarjani, A. Shakouri, J.-H. Bahk, Z. Bian, G. Zeng, J. Bowers, H. Lu, J. Zide, and A. Gossard, “Effect of nanoparticle scattering on thermoelectric power factor,” *Appl. Phys. Lett.* **94**(20), 202105 (2009).
- ²¹J.-H. Bahk, Z. Bian, and A. Shakouri, “Electron energy filtering by a nonplanar potential to enhance the thermoelectric power factor in bulk materials,” *Phys. Rev. B* **87**(7), 075204 (2013).
- ²²S. Foster, M. Thesberg, and N. Neophytou, “Thermoelectric power factor of nanocomposite materials from two-dimensional quantum transport simulations,” *Phys. Rev. B* **96**(19), 195425 (2017).
- ²³H. Yang, J.-H. Bahk, T. W. Day, A. Mohammed, G. J. Snyder, A. Shakouri, and Y. Wu, “Enhanced thermoelectric properties in bulk nanowire heterostructure-based nanocomposites through minority carrier blocking,” *Nano Lett.* **15**, 1349 (2015).
- ²⁴J.-H. Bahk and A. Shakouri, “Enhancing the thermoelectric figure of merit through the reduction of bipolar thermal conductivity with heterostructure barriers,” *Appl. Phys. Lett.* **105**(5), 052106 (2014).
- ²⁵J.-H. Bahk and A. Shakouri, “Minority carrier blocking to enhance the thermoelectric figure of merit in narrow-band-gap semiconductors,” *Phys. Rev. B* **93**(16), 165209 (2016).
- ²⁶S. Foster and N. Neophytou, “Effectiveness of nanoinclusions for reducing bipolar effects in thermoelectric materials,” *Comput. Mater. Sci.* **164**, 91–98 (2019).
- ²⁷S. Ghosh, H. Naithani, B. Ryu, G. Oppitz, E. Müller, and J. de Boor, “Towards energy filtering in Mg_2X -based composites: Investigating local carrier concentration and band alignment via SEM/EDX and transient Seebeck microprobe analysis,” *Mater. Today Phys.* **38**, 101244 (2023).
- ²⁸P. Hohenberg and W. Kohn, “Inhomogeneous electron gas,” *Phys. Rev.* **136**(3B), B864–B871 (1964).
- ²⁹W. Kohn and L. J. Sham, “Self-consistent equations including exchange and correlation effects,” *Phys. Rev.* **140**(4A), A1133–A1138 (1965).
- ³⁰P. E. Blöchl, “Projector augmented-wave method,” *Phys. Rev. B* **50**(24), 17953–17979 (1994).
- ³¹G. Kresse and D. Joubert, “From ultrasoft pseudopotentials to the projector augmented-wave method,” *Phys. Rev. B* **59**(3), 1758–1775 (1999).
- ³²J. P. Perdew, K. Burke, and M. Ernzerhof, “Generalized gradient approximation made simple,” *Phys. Rev. Lett.* **77**(18), 3865–3868 (1996).
- ³³G. Kresse and J. Furthmüller, “Efficient iterative schemes for *ab initio* total-energy calculations using a plane-wave basis set,” *Phys. Rev. B* **54**(16), 11169–11186 (1996).
- ³⁴G. Kresse and J. Furthmüller, “Efficiency of *ab initio* total energy calculations for metals and semiconductors using a plane-wave basis set,” *Comput. Mater. Sci.* **6**(1), 15–50 (1996).
- ³⁵A. V. Krūkav, O. A. Vydrov, A. F. Izmaylov, and G. E. Scuseria, “Influence of the exchange screening parameter on the performance of screened hybrid functionals,” *J. Chem. Phys.* **125**(22), 224106 (2006).

- ³⁶B. Ryu, S. Park, E.-A. Choi, J. de Boor, P. Ziolkowski, J. Chung, and S. D. Park, "Hybrid-functional and quasi-particle calculations of band structures of Mg_2Si , Mg_2Ge , and Mg_2Sn ," *J. Korean Phys. Soc.* **75**(2), 144–152 (2019).
- ³⁷C. G. Van de Walle and R. M. Martin, "Theoretical study of band offsets at semiconductor interfaces," *Phys. Rev. B* **35**(15), 8154–8165 (1987).
- ³⁸R. Shaltaf, G.-M. Rignanese, X. Gonze, F. Giustino, and A. Pasquarello, "Band offsets at the Si/SiO_2 interface from many-body perturbation theory," *Phys. Rev. Lett.* **100**(18), 186401 (2008).
- ³⁹B. Ryu and K. J. Chang, "The electronic properties of the interface structure between ZnO and amorphous HfO_2 ," *Phys. B* **404**(23–24), 4823–4826 (2009).
- ⁴⁰B. Ryu and K. J. Chang, "Defects responsible for the Fermi level pinning in n^+ poly- Si/HfO_2 gate stacks," *Appl. Phys. Lett.* **97**(24), 242910 (2010).
- ⁴¹B. Ryu, "Work function of bismuth telluride: First-principles approach," *J. Korean Phys. Soc.* **72**(1), 122–128 (2018).
- ⁴²R. Vienne, C. Colinet, P. Jund, and J.-C. Tédénac, "Phase stability of ternary antiperovskite type compounds in the quasi-binary systems $\text{Mg}_2\text{X}-\text{Mg}_2\text{Y}$ ($\text{X}, \text{Y} = \text{Si}, \text{Ge}, \text{Sn}$) via ab-initio calculations," *Intermetallics* **31**, 145–151 (2012).
- ⁴³S. Ayachi, R. Deshpande, P. Ponnusamy, S. Park, J. Chung, S. Park, B. Ryu, E. Müller, and J. de Boor, "On the relevance of point defects for the selection of contacting electrodes: Ag as an example for $\text{Mg}_2(\text{Si},\text{Sn})$ -based thermoelectric generators," *Mater. Today Phys.* **16**, 100309 (2021).
- ⁴⁴G. Shi and E. Kioupakis, "Relativistic quasiparticle band structures of Mg_2Si , Mg_2Ge , and Mg_2Sn : Consistent parameterization and prediction of Seebeck coefficients," *J. Appl. Phys.* **123**(8), 085114 (2018).
- ⁴⁵A. Stella, A. D. Brothers, R. H. Hopkins, and D. W. Lynch, "Pressure coefficient of the band gap in Mg_2Si , Mg_2Ge , and Mg_2Sn ," *Phys. Status Solidi B* **23**(2), 697–702 (1967).
- ⁴⁶T. Aizawa, R. Song, and A. Yamamoto, "Solid-state synthesis of thermoelectric materials in $\text{Mg}-\text{Si}-\text{Ge}$ system," *Mater. Trans.* **46**(7), 1490–1496 (2005).
- ⁴⁷L. A. Lott and D. W. Lynch, "Infrared absorption in Mg_2Ge ," *Phys. Rev.* **141**(2), 681–686 (1966).
- ⁴⁸H. G. Lipson and A. Kahan, "Infrared absorption of magnesium stannide," *Phys. Rev.* **133**(3/A), A800–A810 (1964).
- ⁴⁹C. G. Van de Walle and J. Neugebauer, "Universal alignment of hydrogen levels in semiconductors, insulators and solutions," *Nature* **423**(6940), 626–628 (2003).
- ⁵⁰A. Sankhla, H. Kamila, K. Kelm, E. Mueller, and J. de Boor, "Analyzing thermoelectric transport in n -type $\text{Mg}_2\text{Si}_{0.4}\text{Sn}_{0.6}$ and correlation with microstructural effects: An insight on the role of Mg," *Acta Mater.* **199**, 85–95 (2020).
- ⁵¹N. Neophytou, S. Foster, V. Vargiamidis, G. Pennelli, and D. Narducci, "Nanostructured potential well/barrier engineering for realizing unprecedentedly large thermoelectric power factors," *Mater. Today Phys.* **11**, 100159 (2019).
- ⁵²A. Masci, E. Dimaggio, N. Neophytou, D. Narducci, and G. Pennelli, "Large increase of the thermoelectric power factor in multi-barrier nanodevices," *Nano Energy* **132**, 110391 (2024).
- ⁵³V. Vargiamidis and N. Neophytou, "Hierarchical nanostructuring approaches for thermoelectric materials with high power factors," *Phys. Rev. B* **99**(4), 045405 (2019).
- ⁵⁴J. de Boor, T. Dasgupta, U. Saparamadu, E. Müller, and Z. F. Ren, "Recent progress in p -type thermoelectric magnesium silicide based solid solutions," *Mater. Today Energy* **4**, 105–121 (2017).
- ⁵⁵J. de Boor, U. Saparamadu, J. Mao, K. Dahal, E. Müller, and Z. Ren, "Thermoelectric performance of Li doped, p -type $\text{Mg}_2(\text{Ge},\text{Sn})$ and comparison with $\text{Mg}_2(\text{Si},\text{Sn})$," *Acta Mater.* **120**, 273–280 (2016).
- ⁵⁶N. Neophytou, X. Zianni, H. Kosina, S. Frabboni, B. Lorenzi, and D. Narducci, "Simultaneous increase in electrical conductivity and Seebeck coefficient in highly boron-doped nanocrystalline Si," *Nanotechnology* **24**(20), 205402 (2013).
- ⁵⁷P. Graziosi, K.-I. Mehnert, R. Dutt, J.-W. G. Bos, and N. Neophytou, "Materials design criteria for ultrahigh thermoelectric power factors in metals," *PRX Energy* **3**(4), 043009 (2024).
- ⁵⁸B. Ryu, E.-A. Choi, S. Park, J. Chung, J. de Boor, P. Ziolkowski, E. Müller, and S. Park, "Native point defects and low p -doping efficiency in $\text{Mg}_2(\text{Si},\text{Sn})$ solid solutions: A hybrid-density functional study," *J. Alloys Compd.* **853**, 157145 (2021).
- ⁵⁹H. Kamila, B. Ryu, S. Ayachi, A. Sankhla, E. Mueller, and J. de Boor, "Understanding the dopability of p -type $\text{Mg}_2(\text{Si},\text{Sn})$ by relating hybrid-density functional calculation results to experimental data," *J. Phys. Energy* **4**(3), 035001 (2022).
- ⁶⁰S. Ayachi, S. Park, B. Ryu, S. Park, E. Mueller, and J. de Boor, "High-performance thermoelectric devices made faster: Interface design from first principles calculations," *Adv. Phys. Res.* **3**(1), 2300077 (2024).